This is the peer reviewd version of the followng article:

An Aqueous Route to Oxygen-Deficient Wake-Up-Free La-Doped HfO2 Ferroelectrics for Negative Capacitance Field Effect Transistors / Pujar, Pavan; Cho, Haewon; Kim, Young-Hoon; Zagni, Nicolo; Oh, Jeonghyeon; Lee, Eunha; Gandla, Srinivas; Nukala, Pavan; Kim, Young-Min; Alam, Muhammad Ashraful; Kim, Sunkook. - In: ACS NANO. - ISSN 1936-0851. - 17:19(2023), pp. 19076-19086. [10.1021/acsnano.3c04983]

Terms of use:

The terms and conditions for the reuse of this version of the manuscript are specified in the publishing policy. For all terms of use and more information see the publisher's website.

26/12/2024 10:35

(Article begins on next page)

An aqueous route to oxygen-deficient wake-up–free La-doped HfO_2 ferroelectrics for negative capacitance field effect transistors

Pavan Pujar[1, #], Haewon Cho[2, #], Young-Hoon Kim[3, #], Nicolò Zagni[4, #], Jeonghyeon Oh[2] Eunha Lee[5], Srinivas Gandla[2], Pavan Nukala[6,], Young-Min Kim[3,*], Muhammad Ashraful Alam[7,*], Sunkook Kim[2,*]*

[1]Department of Ceramic Engineering, Indian Institute of Technology (IIT-BHU), Varanasi, Uttar Pradesh 221005, India.

[2]Multifunctional Nano Bio Electronics Lab, School of Advanced Materials Science and Engineering, Sungkyunkwan University, Gyeonggi-do, Suwon 16419, Republic of Korea.

[3]Department of Energy Science, Sungkyunkwan University (SKKU), Suwon 16419, Republic of Korea.

[4]Department of Engineering "Enzo Ferrari" (DIEF), University of Modena and Reggio Emilia, Modena 41125, Italy.

[5]Analytical Engineering Group, Samsung Advanced Institute of Technology (SAIT), Samsung Electronics, Suwon, 16678 Republic of Korea.

[6]Centre for Nano Science and Engineering, Indian Institute of Science, Bengaluru, 560012, India.

[7]School of Electrical and Computer Engineering, Purdue University, West Lafayette, Indiana 47907, USA.

[#] Equal Contribution

© 2023 ACS. *This is the version of the article before editing, as submitted to 'ACS Nano'. The Full Article is available online at 10.1021/acsnano.3c04983.*

* Corresponding Authors

Abstract

The crucial role of nanocrystalline morphology in stabilizing the ferroelectric orthorhombic (o)-phase in doped-hafnia films is achieved via chemical solution deposition (CSD) by intentionally retaining carbonaceous impurities to inhibit grain growth. However, in the present study, large-grained (> 100 nm) La-doped HfO_2 (HLO) films are grown directly on silicon by adopting engineered water-diluted precursors with minimum carbonaceous load and excellent shelf-life. The o-phase stabilization is accomplished through well-distributed La dopant, which generates uniformly populated oxygen vacancies, eliminating the need for oxygen-scavenging electrodes. These oxygen-deficient HLOs show a maximum remnant polarization of 37.6 μC/cm^2 ($2P_r$) without wake-up and withstand large fields (> 6.2 MV/cm). Furthermore, CSD-HLO in series with Al_2O_3 improves switching of MOSFETs (with amorphous oxide channel) based on the negative capacitance effect. Thus, uniformly distributed oxygen vacancies serve as a standalone factor in stabilizing the o-phase, enabling efficient wake-up–free ferroelectricity without the need for nanostructuring, capping stresses, or oxygen-reactive electrodes.

Keywords: Ferroelectrics, wake-up–free, negative capacitance, chemical solution deposition,

oxygen vacancy

Introduction

Ferroelectrics possess polarization even when there is no electric field, making them useful in various applications, including three-terminal devices like ferroelectric field-effect transistors and negative capacitance field-effect transistors (NCFETs) (description S1). The ferroelectricity observed in doped-hafnia (HfO_2) makes it CMOS-compatible, and the ferroelectric response becomes prominent at thicknesses ≈ 10 nm.[1, 2] HfO_2 crystallizes in the monoclinic phase ($P2_1/c$, m-phase) at room temperature and standard pressure. At high temperatures and pressures, it exhibits metastable phases, namely, the cubic phase ($Fm\bar{3}m$, c-phase) or tetragonal phase ($P4_2/nmc$, t-phase). These two phases can be stabilized by nanostructuring and doping at room temperature.[3, 4] While the original metastable phases are centrosymmetric and nonpolar, the stabilized orthorhombic ($Pca2_1$, o-phase) and rhombohedral phases ($R3m$, r-phase) are non-centrosymmetric and exhibit ferroelectricity.[3, 4]

The emergence of o-phase is attributed to the formation of sub-10 nm grains owing to its lower volume compared to the m-phase.[1, 2, 3] Numerous attempts were reported to crystallize doped-HfO_2 with nanostructured morphology, especially in the case of films from atomic layer deposition (ALD) and chemical solution deposition (CSD).[4, 5] [J. Mater. Chem. C 8, 2820 (2020), 10.1149/2.0061512jss, Appl. Phys. Lett. 117, 212904 (2020), 10.35848/1347-4065/aba50b, https://doi.org/10.1016/j.ceramint.2017.05.181, https://doi.org/10.1002/admi.202100907, 10.7567/JJAP.57.11UF06] Former is known to deposit robust monolayers and latter is mainly employed to grow thicker films.[6, 7, 8] In both the cases, a prominent mechanism of inhibiting the grain growth, i.e., kinetic stabilization of o-phase is used.[9] The retained carbonaceous impurities arising from the incomplete oxidation of precursor, serves as a growth inhibitor.[10, 11] However, the

presence of small grains, i.e., large grain boundary area with carbon segregation, leads to high leakage currents and low electrical breakdown.[5, 12] Despite being cost-effective and having high yield, with greater processing controllability for a wide range of chemical compositions, CSD-processed films (with grain-boundaries decorated by carbonaceous impurities) face challenges in commercialization because the resulting film is not suitable for industry-grade application. Specifically, although CSD has been consistently used to produce electronic-grade oxides over the years, its efficacy in developing robust HfO_2-ferroelectics is not fully understood except few attempts on thicker films (e.g., 390 nm)[8] with small grains (radius ≈ 10 nm) via a mechanism similar to ALD.

Moreover, there have been no reports on ferroelectric phase stabilization in carbon–inhibitor-free doped-HfO_2 films or the related microscopic mechanism and no attempts have succeeded in extending CSD to ultrathin films (< 15 nm), despite their requirement for ultradense nanoelectronics.[13] Herein, both the thickness and carbon-impurity issues mentioned above are addressed by engineering precursors with minimum carbon-load and depositing phase-pure ultrathin films directly on silicon. Further, lanthanum (La) is proven to be a very suitable stabilizer of ferroelectric o-phase, predicted by density functional theory and La-doped HfO_2 (HLO) films have experimentally shown robust ferroelectricity.[6, 14] Herein, CSD-mediated HLO ferroelectric films are deposited on silicon using chloride and nitrates as the Hf and La sources, respectively; the solvent used to form homogeneous and pure precursors is a mixture of miscible 2-methoxyethanol (2-ME) and water (Aq). Simple inorganic salts are easily decomposed and provide better film quality, and hence are preferred over long-chain carbonaceous ligands. A large-aqueous fraction in precursors allows films to be free of carbon inhibitors and La-doping results in uniform distribution of intrinsic oxygen (O) vacancies[15], which is harnessed to maximize polarization

charge. These aqueous CSD-processed HLO thin films are further integrated with Al_2O_3 in the gate stack of amorphous indium gallium zinc oxide (IGZO)–channel MOSFETs to improve the electrical characteristics in terms of output current (I_{ON}) and subthreshold swing (SS) through negative capacitance (NC) effect.

Results and Discussion

Ferroelectricity in large-grain CSD-HLO thin film on silicon

HLO thin film directly grown on silicon without a buffer-metal, makes it CMOS-compatible (**Fig. 1a**). No capping-electrode-induced stresses were used to stabilize the desired ferroelectric o-phase. The precursor was composed of a co-solvent (2-ME and Aq, designated as [2-ME+Aq], hereafter) with large (62.5 vol.%) of Aq. Presence of small fraction of 2-ME reduces the surface tension of precursor, promoting easy spread of precursor on silicon; multiple spin-deposition and thermal annealing steps were found advantageous in growing amorphous HLO films, and their crystallization using rapid thermal annealing (RTA) was helpful to achieve o-phase (**Fig. 1b**). 2-ME+Aq precursor was also efficient in atomic-level mixing of Hf and La-sources resulting in the uniform distribution of La throughout the film thickness (**Fig. 1c**), thus, effect of La^{3+} was isotropic. The choice of Hf-chloride ($HfCl_4$) and La-nitrate ($La(NO_3)_2$) as cation sources in aqueous medium was to minimize the carbon load. However, since carbon sourced from the small fraction of 2-ME was effectively removed by annealing, this led to impede-free grain growth (> 100 nm) (**Fig. 1d**). Further, **Fig. 1e** shows the polarization vs. electric field (*P* vs. *E*) loop of a ≈ 35-nm HLO layer inserted between silicon and Mo-metal forming a two-terminal capacitor, from which remnant polarization ($2P_r$) of 37.6 μC/cm^2 and coercive field (E_C) < 4 MV/cm are extracted. The wake-up–free, stable $2P_r$ is observed under cyclic electric field (2×10^6 times) (**Fig. 1f**). The

P–E loop is fitted with Landau-Khalatnikov equation generalized to include the dielectric contribution of co-existing non-polar phases in the HLO film [16] (**Fig. 1e** and description S1).

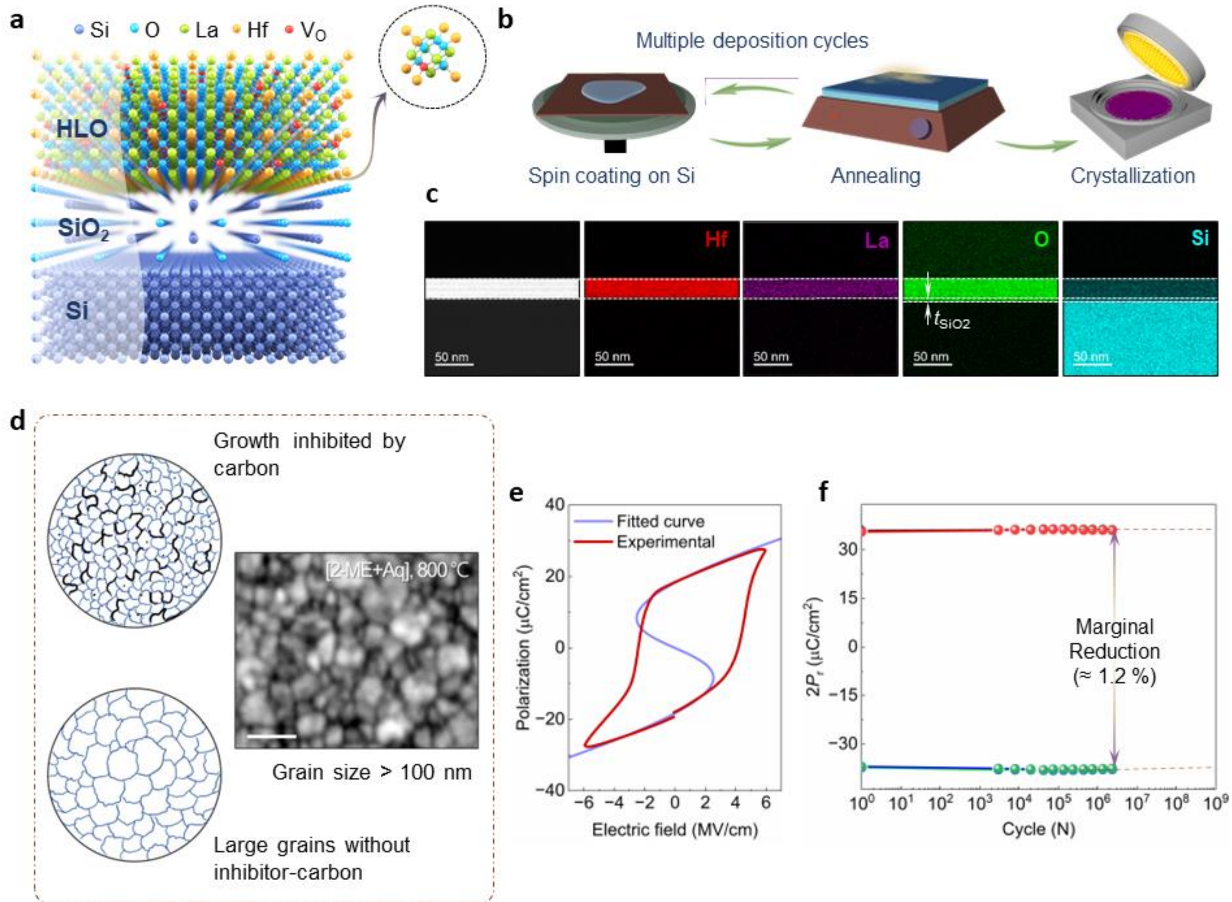

Figure 1. Aqueous CSD-processed HLO thin film on silicon. Schematic of **a** Si/SiO_2/HLO structure and **b** solution deposition and annealing processes. **c** Nanoscale elemental distribution mapping for the HLO film (La~7.4 %) deposited from [2ME+Aq] precursor crystallized at 800 °C. **d** Schematic presenting the effect of carbon inhibitors in growing small grains and absence of which leads to large grain size; Band contrast image of electron backscatter diffraction (EBSD) analysis for grain size measurement of [2-ME+Aq] HLO thin film crystallized at 800 °C (scale bar: 300 nm). **e** Ferroelectric polarization measurements of Si/HLO(≈ 35 nm)/Mo capacitors fitted with generalized Landau-Khalatnikov equation. **f** Effect of electric field cycling on the ferroelectric polarization of [2-ME+Aq] HLO thin film.

Deposition strategy and thickness-dependent phase evolution

The decomposition of precursor to form desired –Hf–O–La– network is initially probed using thermogravimetric analysis (TGA) and differential thermal analysis (DTA), the recorded thermal traces of precursors determine the minimum annealing temperature (T_a). The temperature at which the TGA curves reach a horizontal plateau is the minimum T_a (≈ 350 °C) (Fig. S1a-b). Annealing at 350 °C eliminates solvent and bridging ligands, thus reducing the film volume. The repeated deposition-and-annealing cycles build a stack of ultrathin films of same thicknesses, evident from the linear growth (Fig. S2). This conveys the effective replication of single-layer thickness with successive deposition cycles. The subsequent deposition-and-annealing cycles do not affect the underlying film thickness, because the layers-beneath have already undergone a complete transformation to HLO (Fig. S3). Thus, the primary building block of the stack (i.e., the single deposited layers) is free from impurities (C, Cl, and N). The EELS analysis for the ligand-induced impurities confirms the compositional purity (Fig. S4-S5). Notably, the presence of carbonaceous impurities was considered essential to inhibit grain growth. However, this leads to an inconsistent reduction in thicknesses of the preceding layers when deposited in multiples. The systematic growth of layers to yield the desired film thickness standardizes CSD by ensuring thickness reproducibility. Thus, the choice of chloride- and nitrates along with the low molarity (83 mM) simplifies the prediction of the number of layers to be deposited.

Amorphous films derived from these precursors were crystallized via RTA at 700 and 800 °C and their phase evolution was investigated using grazing incidence x-ray diffraction (GIXRD) (**Fig. 2a-d**). Films (< 20 nm thick) deposited from the pure 2-ME precursor were amorphous at

700 °C. In contrast, thicker films show diffraction peaks (**Fig. 2a**, zoomed). Both the 27- and 35-nm-thick films show characteristic (111) reflection of the o/t/c-phases at ≈ 30.6° (2θ), and with increasing film thickness, two signature peaks correspond to the ($\bar{1}$11) and (111) reflections of the m-phase appear at 28.4° and 31.6°, respectively.[3, 6] On increasing the RTA temperature (800 °C for 60 s), the films in the ultrathin regime (thickness < 20 nm) show diffraction signatures of the o/c/t-phases. For the ≈ 35 nm HLO film crystallized at 800 °C, the averaged grain size from electron backscatter diffraction was estimated to be ≈ 119 ± 33 nm (Fig. S6).

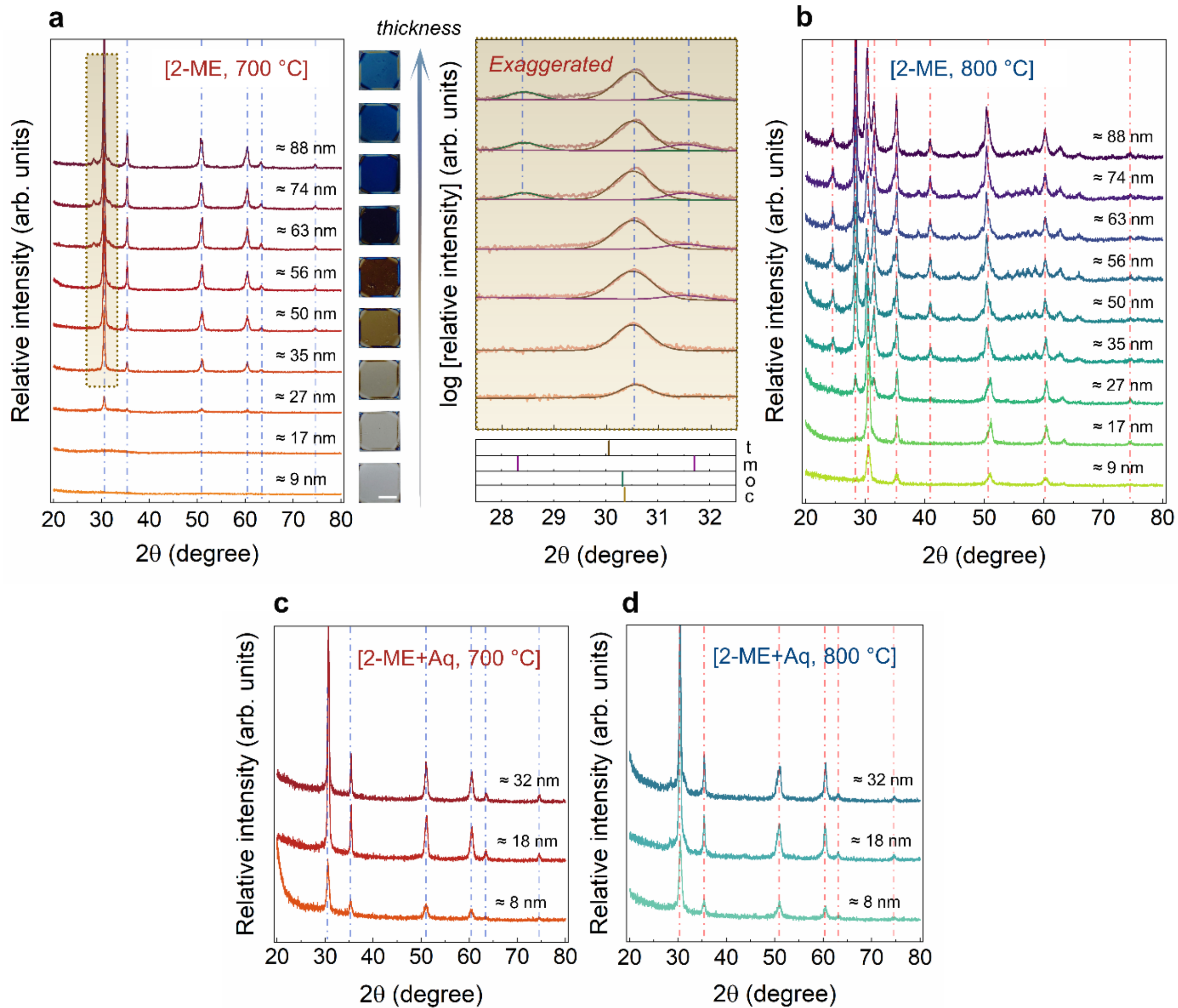

Figure 2. Structural characterization of HLO films grown on silicon. GIXRD patterns of CSD-processed HLO films of different thicknesses (note: the notation used to describe the processing

conditions is [solvent-used, RTA-temperature], where RTA-temperature represents the crystallization temperature): **a** [2-ME, 700 °C], with an exaggerated view of a selected range of patterns at a logarithmic relative intensity scale, where t, m, o and c represents tetragonal, monoclinic, orthorhombic and cubic phases, respectively. Photographs of film surfaces (scale: 1 cm) presenting the variation in color with increasing thickness, **b** [2-ME, 800 °C], **c** [2-ME+Aq, 700 °C] **d** [2-ME+Aq, 800 °C].

Replacing some of the 2-ME with synergistically-effective solvent-water has advantages such as moisture-insensitiveness and, interchanging of strong covalent bonds of 2-ME by weak electrostatic interaction between metal cations and aqua ions.[17] Additionally, high molecular weight 2-ME is comparatively more viscous than water and requires thermal driving force to evaporate, whereas water quickly evaporates but results in poor morphology.[18] With this trade-off in mind, a co-solvent comprising water and 2-ME (5:3 v/v) was further adopted. With a large fraction of water, more coating steps are required to achieve a thickness similar to that of 2-ME-based precursor (Fig. S2). Irrespective of RTA temperature, [2-ME+Aq] films were found to crystallize in o/c/t-phases (**Fig. 2c-d**). Furthermore, the roughness of HLO films was found < 0.5 nm presenting their device-integrable quality (Fig. S7a-c).

Overall, the GIXRD results indicate that the crystallinity of the HLO films on Si/SiO_2 improves with increasing thickness. Notably, the films grown using 2-ME+Aq-based precursor show a single-phase configuration, even at a thickness of ≈ 9 nm. Due to the structural similarities of the c–, t–, and o–phases,[19, 20] an extended investigation using atomic-resolution scanning transmission electron microscopy (STEM) combined with position-averaged convergent beam electron diffraction (PACBED) and energy dispersive X-ray spectroscopy (EDX) was utilized.[19, 21, 22]

Structural and chemical analysis

Three ≈ 35 nm thick HLO films, [2-ME, 700 °C/800 ºC] and [2-ME+Aq, 800 ºC] were analyzed by high-angle annular dark field (HAADF) STEM. Low-magnification HAADF STEM images of each film are shown in **Fig. 3a–c**. Nanoscale EDX maps of the three samples (**Fig. 1c** and Fig. S8) reveal that La is uniformly substituted for Hf-host without segregation and that doping concentration is ≈ 7 % relative to the Hf. These observations, made from a relatively large field-of-view, demonstrate that the HLO films grew uniformly with a flat surface regardless of the solvent. To determine the crystal structure of the major phase in HLO films, atomic-resolution HAADF STEM imaging was performed (**Fig. 3d–f**). The images exactly match the atomic models of orthorhombic structure proving it to be the major phase, which supports the macroscopic GIXRD interpretations. Additional fast Fourier transform (FFT) and PACBED analyses[21] on the same regions verify the formation of the o-phase (Fig. S9). Note that the m-phase in the HLO [2-ME, 800 °C] sample is not observed within the TEM observation scale due to its small phase fraction.

A notable difference between the two different treatments [2-ME] and [2-ME+Aq] adopted for HLO growth was found from atomic-resolution STEM-EDX mapping.[23, 24] According to elemental distribution maps of Hf (purple) and La (green) obtained for the two different HLO films annealed at 800 °C (**Fig. 3g-h**), Hf and La atoms are inhomogeneously distributed in the HLO [2-ME] film, whereas they are uniformly distributed in the HLO [2-ME+Aq] film. This suggests that the local chemical composition differs in the HLO [2-ME] film. **Fig. 3i** represents the standardless quantification of La content at different locations on both [2-ME] and [2-ME+Aq] HLOs. This

depicts compositional fluctuation of La dopants mainly in [2-ME] HLOs, while [2-ME+Aq] HLOs present a well-maintained dopant concentration of ≈ 7 %.

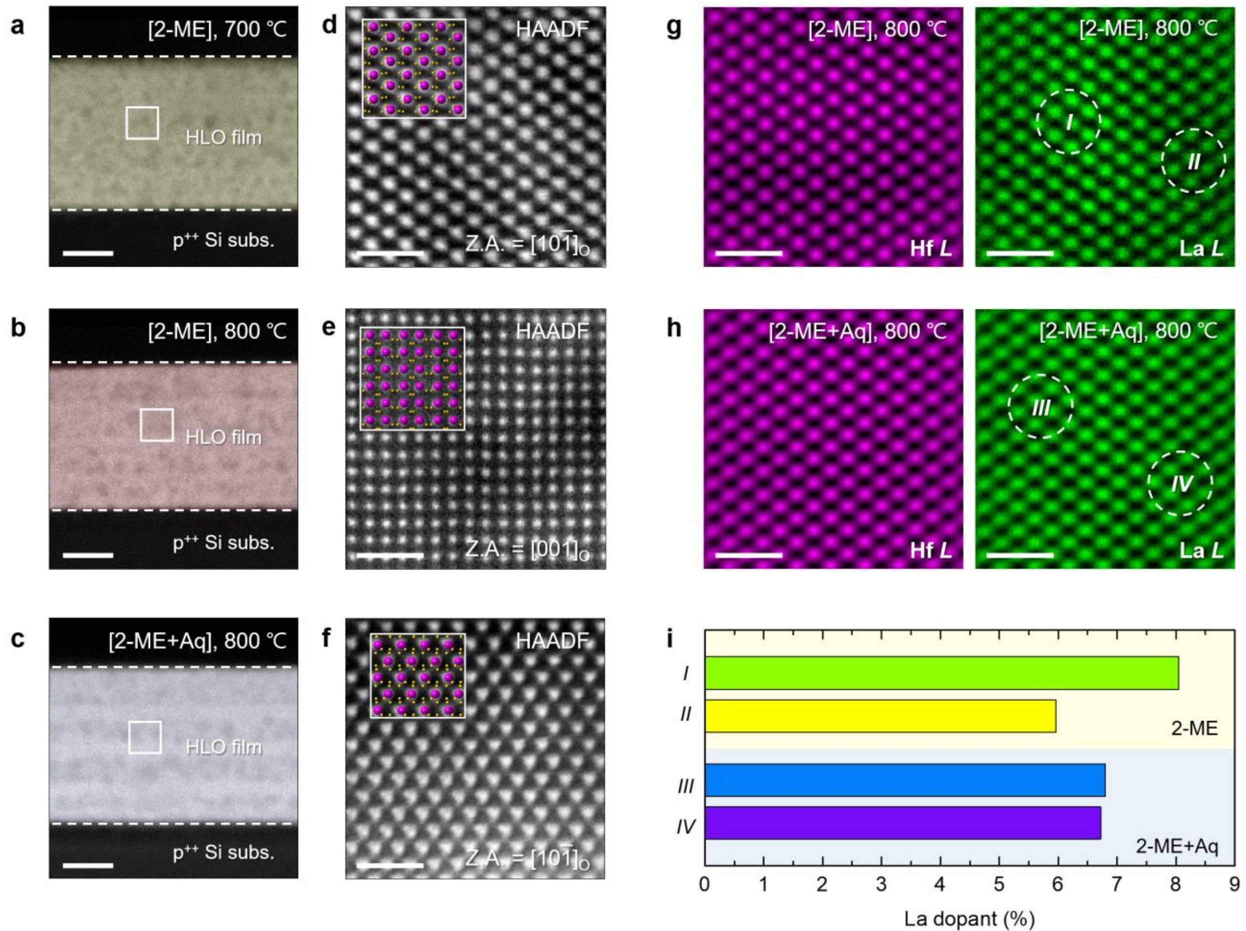

Figure 3. Atomic structures and site population of La dopants. **a–c** Low-magnification HAADF STEM images of HLO [2-ME, 700 °C], [2-ME, 800 °C], and [2-ME+Aq, 800 °C] films, respectively. Scale bars are 10 nm. **d–f** Atomic structure images of the three regions marked by white squares in the three HLO films. The three regions chosen for atomic structure observation were aligned to the crystal zone axis of [10$\bar{1}$] or [001], and the corresponding atomic models (Hf: purple ball, O: dark yellow ball) show an excellent match with the atomic-resolution HAADF STEM images. Scale bars are 1 nm. (**g, h**) Atomic-resolution STEM-EDX maps of the cations Hf (purple) and La (green) in the HLO [2-ME, 800 °C] and [2-ME+Aq, 800 °C] samples. Scale bars are 1 nm. Characteristic X-ray peaks of Hf L (7.898 keV) and La L (4.650 keV) were selected for elemental mapping. **i** Standardless quantification of the La concentration for the four regions I–IV

marked in the two La maps.

Oxygen vacancy distribution in orthorhombic phase

Compositional inhomogeneity of La^{3+} in the HLO [2-ME] film results in local variation in distribution of O-vacancies introduced for charge compensation.[21, 22] In contrast, O-vacancies are expected to be evenly distributed in the HLO [2-ME+Aq]. We conducted O *K* electron energy loss spectroscopy (EELS) spectrum imaging (SI) to analyze the spatial distribution of O-vacancies. O-vacancies lower local crystal symmetry, affecting relative distance between Hf and O atoms, thus resulting in modification of the hybridized O 2*p*–Hf 5*d* orbital states due to defect states, symmetry breaking, and charge redistribution.[21] As the concentration of O-vacancies increases, the unoccupied states above the conduction band shift to lower energy levels and change the shape of the pre-peak of the O *K* edge. The modification results in a reduction of the hybridized O *2p*-Hf de_g states in comparison to the hybridized O *2p*-Hf dt_{2g} states. In other words, the relative intensity (*A/B*) of the first peak *A* with respect to the second peak *B* in the O *K* edge decreases as the content of O-vacancies increases due to the formation of shallow donor states below the conduction band (**Fig. 4a–c**). [21, 25] Studies have shown that typical doublet peak shape of the O *K* edge in doped-HfO_2 changes depending on the type of crystal phase, crystallinity, annealing condition, structural disorder, and concentration of O-vacancies.[26, 27] Considering that the HLO films were grown with the same growth method to form a highly crystalline o-phase as a major phase, simple monitoring of the change in the *A*/*B* ratio in the O *K* EELS edge can convey the variation in the vacancy content. By multiple-linear/non-linear least squares (M/NLLS) fitting to the O *K* EELS SI data, which outputs Gaussian curve fits of the *A/B* distribution,[28] spatial maps of the *A*/*B* ratios were

obtained for the three HLOs (**Fig. 4d–f**). For the HLOs [2-ME, 700/800 ºC], the *A*/*B* ratios are revealed to locally differ, indicating that O-vacancies in the films are inhomogeneously distributed. This result strongly supports the inference from the STEM-EDX maps that La dopants were unevenly substituted at Hf sites. Comparing histograms of the *A*/*B* ratios for the two HLO [2-ME] samples shows that the O-vacancies become more highly localized in the sample annealed at 800 °C (i.e., wider FWHM). In contrast, HLO [2-ME+Aq] shows remarkably different vacancy distribution. The HLO [2-ME+Aq] film is homogeneously populated by O-vacancies over the entire film with large vacancy content, which is correlated with the uniform doping of La revealed by STEM-EDX. This result suggests that the Aq-based precursor is substantially effective in forming the o-phase with a high density of homogeneously distributed O-vacancies.

These additional O-vacancies in [2-ME+Aq, 800 ºC] HLO is attributed to the presence of negatively charged hydroxides (OH^-) owing to large fraction of Aq in the precursor, which reduces the valence of Hf (< 4) and gives rise to the formation of higher concentration of suboxides ($HfO_{(x < 2)}$) accompanied by O-vacancies. The analysis of the same is probed using x-ray photoelectron spectroscopic measurements (description S2 and Fig. S10). Further, earlier reported attempts of stabilizing the o-phase through O-vacancies have adopted a strategy of removing oxygen from the film by oxygen-reactive capping electrodes (e.g., titanium nitride). These electrodes scavenge oxygen from the film and result in formation of unfavorable intermediate oxide layers (e.g., TiO_xN_y or TiO_x)[4]. In contrast, the present CSD strategy allows HLO thin films on silicon to achieve considerable fraction of well-distributed O-vacancies without capped electrodes. Based on a recent report revealing the role of O-vacancies in ferroelectricity enhancement,[21] HLO [2-ME+Aq] film is expected to show prominent ferroelectricity.

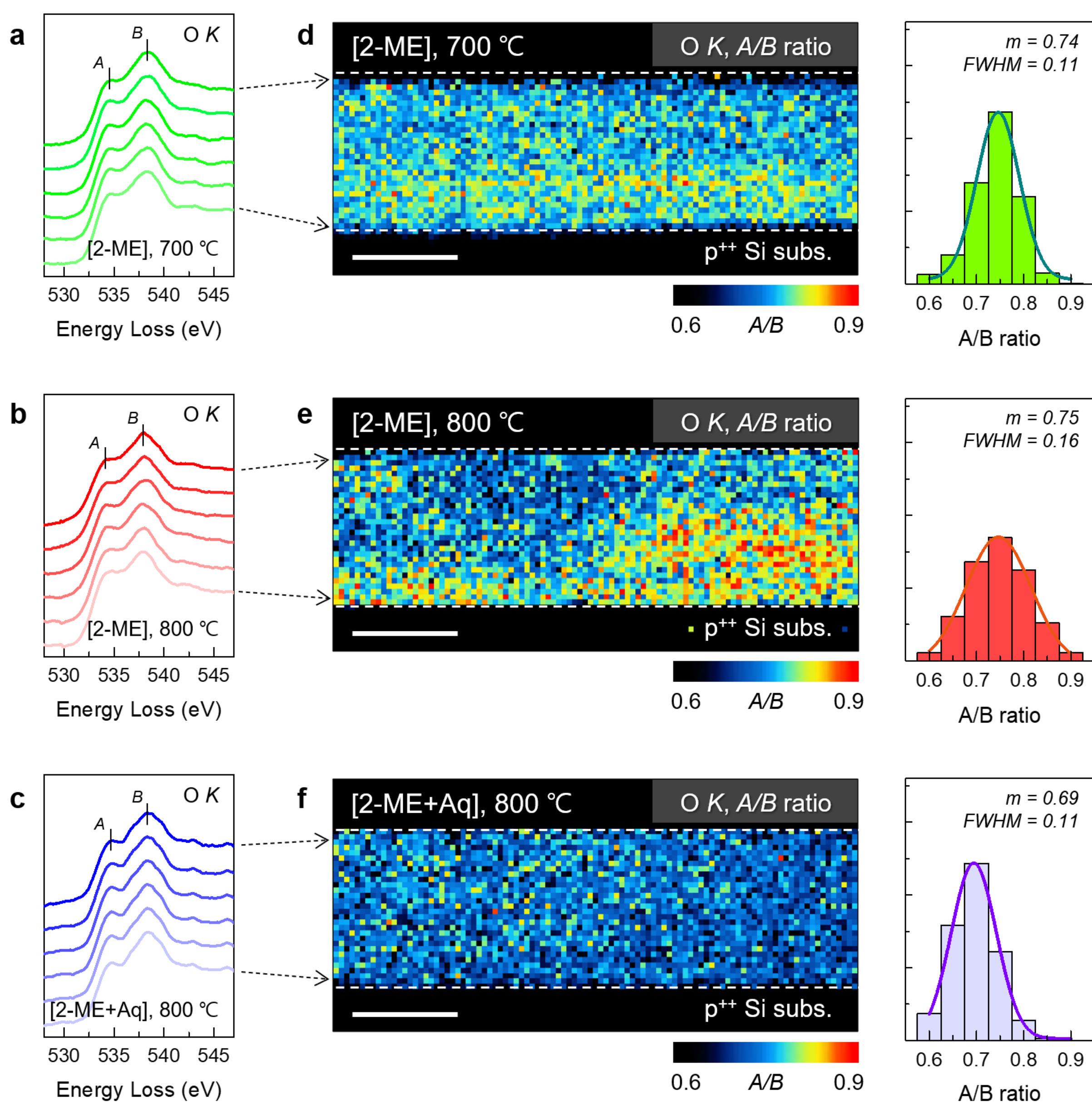

Figure 4. Oxygen vacancy distribution analysis. **a–c** Representative O K edges extracted from the bottom to the top in the three HLO [2-ME, 700 °C], [2-ME, 800 °C], and [2-ME+Aq, 800 °C] films. **d–f** Maps of the A/B ratio in the O K edge, reconstructed by M/NLLS fitting to the O K edge corresponding to each pixel in the experimental EELS SI data for the three HLO samples. The color scales shown at the bottom right of each map indicate the range of the measured A/B ratio. Scale bars are 20 nm. The histograms shown on the right side represent the distributions of the measured A/B ratios for the three samples. Note that the statistical distributions of the A/B ratios in the HLO [2-ME+Aq] film are smaller and narrower than those in the HLO [2-ME] films

annealed at 700 and 800 °C. Note that m and FWHM stand for mean value and full-width-half-maximum of the Gaussian peak.

Ferroelectric polarization measurements

Assessment of the ferroelectricity in Si/HLO/Mo capacitors was carried out through polarization switching measurements at 1 kHz. **Fig. 5a-b** presents *P–E* hysteresis loops for Si/HLO/Mo capacitors with ≈ 35 nm HLO films deposited from the 2-ME–based precursor and crystallized at 700 and 800 °C. The obtained P_r values range from 16.7 to 21.2 μC/cm^2 across all annealing temperature, with the maintained E_C of 3 to 5 MV/cm, which is within the range reported for HfO_2 ferroelectrics.[4] However, the P_r values are found to decrease with thickness increasing to ≈ 55 nm (Fig. S17 and Table S21). This decrease is attributed to the appearance of the m-phase (**Fig. 2b-c**). In contrast, the P_r and E_C for [2-ME+Aq, 700 °C] HLO are on the order of 14.4 μC/cm^2 and < 4 MV/cm, respectively; with an increase in the crystallization temperature from 700 to 800 °C, a sharp increase in P_r (= 18.4 μC/cm^2 and $2P_r$ ≈ 37.6 μC/cm^2) is noted (Fig. S17 and Table S21).

The large ferroelectric polarization observed in 2-ME+Aq-derived HLO thin films motivated us to investigate its dependency on the aging of the precursor (Fig. S18). The GIXRD measurements on the film deposited with aged precursor show pure o-phase and the recorded polarization switching depicts no change in the $2P_r$ (≈ 37 μC/cm^2) (Fig. S18a-b); these results convey excellent shelf-life.

Furthermore, for all capacitors, switching currents are found to be on the order of ≈ 90–100 μA (**Fig. 5a-c**). The measured *P–E* curves are slightly asymmetric with larger E_C, which can be attributed to the presence of SiO_2 interfacial layer contributing to a built-in potential. Furthermore, these measured P_r values are larger than those previously reported for CSD-HLOs;

45 nm CSD-processed HLO with 5 cat. % La showed a maximum P_r of 7 μC/cm^2 with a layer-by-layer (L/L) crystallization treatment.[29] The use of a dilute precursor (< 0.1 M) and L/L crystallization is argued to yield better ferroelectric performance for HLO films derived from Hf-acetylacetonate ($Hf(C_5H_7O_2)_4$) and La-acetate ($La(CH_3CO_2)_3$)-based precursors.[29, 30] However, these films have a strong wake-up dependence due to retained carbon. On the contrary, the present CSD-HLOs have relatively large La fraction (≈ 7 %) that is helpful in increasing the O-vacancy concentartion. Additionally, the inhibitor-free recipe led to pure thin films, thus the observed ferroelectricity does not require wake-up.[31]

Owing to the near-complete transformation of precursors into HLO, the capacitors withstand a higher voltage (> 22 V i.e., > 6.2 MV/cm) than most CSD- and ALD-processed doped HfO_2 films without breakdown (**Fig. 5a-c**).[5, 29, 30] For the case of the HLO [2-ME, 700/800 °C] films, especially in the negative bias regime, typical polarization-dependent leakage (beyond 6 MV/cm) is observed as the warping of loop tips. Such leakage and nonferroelectric contributions are further nullified and more reliable P_r values are obtained using positive up negative down (PUND) measurements (Fig. S19-S20 and description S4).[32, 33] The PUND results demonstrate that the onset of actual ferroelectric switching is above 10 V for HLO [2-ME, 700 and 800 °C] (i.e., an E_C of 2.5 MV/cm) and above 12 V for HLO [Aq+2-ME, 800 °C] (i.e., an E_C of 3 MV/cm) for fixed pulse delay and width (= 10 μs).

Furthermore, both 2-ME and 2-ME+Aq-based HLOs were subjected to electric field cycles (at a frequency of 1 kHz); the details of the test parameters are presented in description S5. Although $2P_r$ for both the cases is found to vary marginally with electric field cycles, [2-ME+Aq, 800 °C] HLO is more stable with negligible change in $2P_r$ (**Fig. 1f** and **Fig. 5d-e**). Additionally at different test frequency of 100 Hz, HLO thin films found to exhibit stable $2P_r$ irrepsective of type

of precursor used (Fig. S23). This behavior can be attributed to O-vacancies and their distribution. It has been previously observed that charged defects such as O-vacancies induce nonuniform electric field throughout the film thickness.[4] With an increase in the electric field cycles, the O-vacancies tend to diffuse or drift resulting in uniform distribution of the electric field. Thus, owing to homogeneously populated O-vacancies in the case of [2-ME+Aq, 800 °C] HLOs, it is expected to show better resistance to electric field cycling with negligible reduction in polarization. Further, the present HLO films were compared with the reported La-doped HfO_2 thin films and a table detailing the properties are shown in Table S22

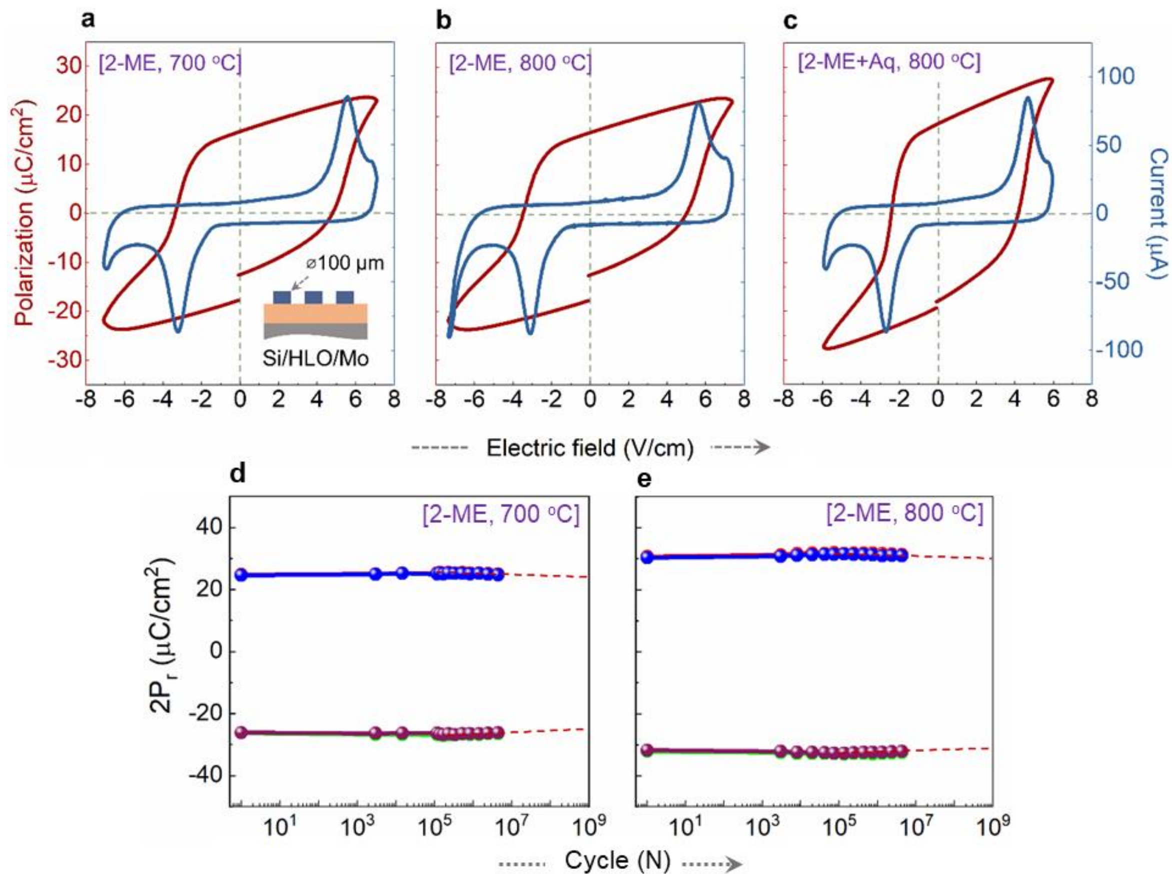

Figure 5. Ferroelectric polarization and stability analysis of Si/HLO/Mo capacitors. Polarization vs. electric field (P vs. E) hysteresis loops of HLO films deposited using the 2-ME-based precursor and crystallized at **a** 700 °C and **b** 800 °C. **c** P vs. E hysteresis loops of HLO films

deposited using the 2-ME+Aq-based precursor and crystallized at 800 °C. Stability of CSD-HLOs under electric field cycling. Endurance behavior of (a) ≈ 35 nm HLO [2-ME, 700 ºC] (b) ≈ 35 nm HLO [2-ME, 800 ºC] at a frequency of 1 kHz and an input voltage of 15 V (i.e., an E_C of 4.7 MV/cm).

HLO-based NCFETs: characterization and simulation

Fig. 6a shows schematic of bottom gate top contact (BGTC) NCFET with CSD-HLO thin film and IGZO–channel. The benefit of HLO in the gate stack with Al_2O_3 is assessed through SS reduction and enhancement in I_{ON}, thanks to the NC effect.[34] **Fig. 6b-c** shows a comparison between HLO-based NCFETs and Al_2O_3-based MOSFETs with low leakage current ≈ 10 pA. **Fig. 6d** shows the SS vs. V_{GS} for NCFET and MOSFET during the forward sweep with a slow V_{GS} sweeping rate, showing a reduction of the minimum value from 92.6 to 86.7 mV/dec. However, with the increase in the sweeping rates, the SS magnitudes achieved sub-thermionic (Fig. S24). Further, NC effect is also realized in the improvement of I_{ON} from 3.85×10^{-7} for the Al_2O_3 to 8.19×10^{-7} A for the HLO. (**Fig. 6e**). The simultaneous SS decrease and I_{ON} increase obtained by the HLO device compared to the MOSFET is evidence of the negative capacitance effect [Pahwa 2016, Kobayashi 2018, Cao 2020]. In practice in fact, it is more feasible to design NCFETs to reduce SS degradation due to short-channel effects as well as increase energy savings thanks to the increased drain current above threshold rather than aiming at reducing SS below 60 mV/dec. Furthermore, the CSD precursors interact with the substrate-Si and on thermal annealing they tend to form ow permittivity-SiO_x layer at the interface between Si and HLO adversely affecting NCFET performance. The integration of a low permittivity dielectric in series with the ferroelectric layer results in a reduced internal voltage amplification effect, therefore counterbalancing the improvements provided by the ferroelectric layer itself.

The improvements in SS and I_{ON} were probed using numerical device simulations. The same geometrical parameters of the actual device were employed in the simulated structure (**Fig. 6a**). The simulation results are shown in **Fig. 6f-i**, with every single panel reporting the corresponding simulated curves to the experimental ones shown in **Fig. 6b-e**. Calibration of the simulation deck was done against the Al_2O_3 MOSFET I_D-V_{GS} curve. The NCFET was then simulated as a series connection between the Al_2O_3 MOSFET and the HLO capacitor (description S6). Four different HLO thicknesses were used (**Fig. 6f, 6h** and **6i**). Simulations predict an improvement in terms of SS and I_{ON} when increasing HLO thickness, in qualitative agreement with the experimental findings. However, quantitatively, simulations predict a much larger improvement for the HLO NCFET compared to the Al_2O_3 MOSFET for both SS and I_{ON}. This could be due to the charge mismatch between the electron density in the IGZO layer and the polarization charge on the HLO, which in general is caused by: i) a large fraction of polarization charge being screened by traps in the gate stack, and ii) the HLO operating in a non-saturated *P*–*E* loop[35] [10.1557/s43578-021-00420-1, 10.1109/JPROC.2023.3234607]. In the simulated devices instead, electrical connection between the Al_2O_3 MOSFET gate and the HLO layer forces the IGZO charge and the polarization to be balanced, hence leading to an enhanced NC effect. In this sense, simulation results need to be interpreted as maximum theoretical limits of the HLO NCFET assuming that polarization charge is fully screened by the channel electron density and that the ferroelectric operates in the saturated *P*–*E* loop.

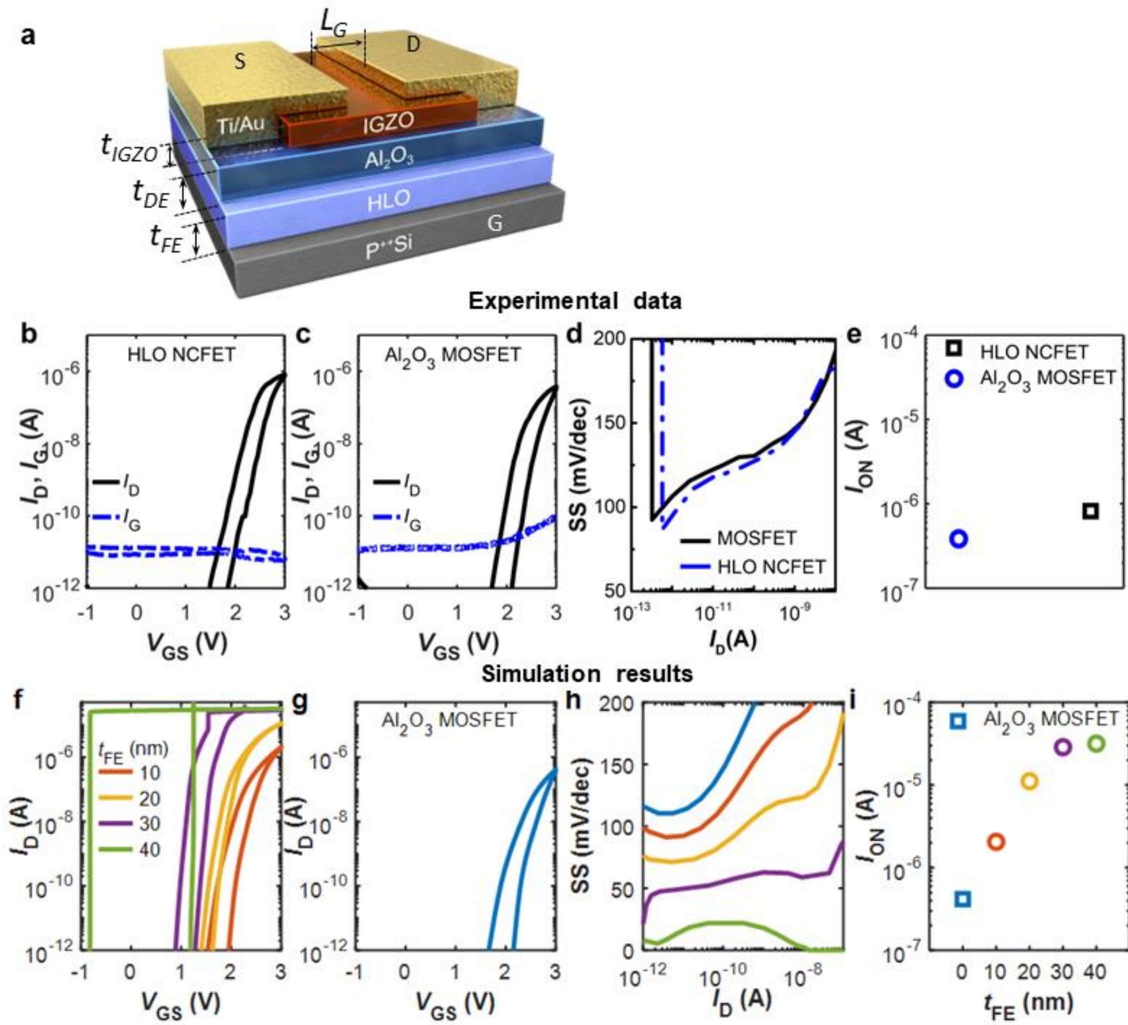

Figure 6. Experimental and simulation results of Al_2O_3 MOSFET and HLO NCFET. **a** Schematic of NCFET architecture. The BGTC transistors consist of CSD-HLO and Al_2O_3 thin films connected in series to fetch their application as a ferroelectric negative capacitor. **b, c** Measured I_D-V_{GS} curves of the HLO NCFET and Al_2O_3 MOSFET, respectively. **d** Measured SS-V_{GS} curves during forward sweep of both devices. **e** I_{ON} of HLO NCFET and Al_2O_3 MOSFET, extracted from I_D-V_{GS} at V_{GS} = 3 V. **f** Simulated I_D-V_{GS} curves of the HLO NCFET for HLO thicknesses (t_{FE}) of 10, 20, 30, 40 nm. **g** Simulated I_D-V_{GS} curve of the Al_2O_3 MOSFET. Simulation parameters were calibrated to reproduce the curve shown in panel (c). **h** Simulated SS-V_{GS} curves during the forward sweep of both devices. **i** I_{ON} of HLO NCFET and Al_2O_3 MOSFET, extracted at the same conditions as for the experimental values.

To summarize, we demonstrated that CSD-processed La-doped-HfO_2 ferroelectrics show o-phase with maximum $2P_r$ of ≈ 37.6 μC/cm^2 at 1 kHz. The water-diluted organic precursors with minimum carbon allowed grain growth (> 100 nm) which greatly controls the leakage current. Microscopy and spectroscopy reveal that the inherent O-vacancies in HLO and their distribution promote stabilization of the o-phase and polarization switching is intertwined with the rich oxygen vacancy charge dynamics.[36] The conventional small-grain morphology, capping stresses and pre-metallized substrates are not necessary, so that water-based CSD yields wake-up–free robust ferroelectric HLO directly on Si/SiO_x. CSD-HLO in a regular gate stack of IGZO MOSFETs has been simulated and demonstrated experimentally to lower SS and enhance I_{ON}, thanks to the NC effect.

EXPERIMENTAL SECTION

Precursor analysis:

Precursor formulation and decomposition: All chemical reagents were purchased from Sigma–Aldrich and used as received without additional purification. Two sets of precursors (85 mM) were formulated using (a) 2-ME and (b) the co-solvent of 2-ME and water (2-ME+Aq). For both precursors, hafnium chloride ($HfCl_4$) and lanthanum nitrate ($La(NO_3)_2$) were used as the Hf and La sources, respectively. For the 2-ME-based precursor, $HfCl_4$ and $La(NO_3)_2$ were each dissolved in 4 ml of 2-ME and then mixed. Similarly, for the 2-ME+Aq-based precursor, $HfCl_4$ was dissolved in 5 ml of deionized water, $La(NO_3)_2$ was dissolved in 3 ml of 2-ME, and they were then mixed; both precursors were vigorously stirred overnight in air. The formulated precursor solutions were stored for 60 days in air-tight bottles to examine their environmental stability and aging. The decomposition pathway of both precursors was probed using thermogravimetric analysis (TGA, Seiko Exstar 6000, TG/DTA6100) and differential thermal analysis (DTA) with a temperature

ramp-up rate of 10 °C/min.

Thin film analysis:

Thin film deposition, thickness validation and surface topography analysis: To deposit thin films of HLO, the precursors were spin-coated at 3000 rpm for 30 s on Si (p++) substrates. Before the deposition process, the silicon wafers were firstly cleaned and then treated with oxygen plasma for 60 s at 60 W. The desired film thicknesses were achieved by multiple coating cycles with intermediate annealing (350 °C for 15 min) steps. The final stack of layers was subjected to hot plate annealing for 2 h at 350 °C. For crystallization, the films were subjected to rapid thermal annealing (RTA, heating rate ≈ 10 °C/s) at 700 and 800 °C for 60 s. The film thickness and surface roughness were analyzed using cross-sectional field-emission scanning electron microscopy (FESEM: JSM-6700F, Hitachi) and atomic force microscopy (AFM: XE7, Park Systems), respectively.

Structural and chemical analysis: Structural characterization of the thin films was performed using grazing incidence X-ray diffraction (GIXRD, D8 DISCOVER) using a Cu Kα source (wavelength: 1.5406 Å) with an incident angle of 0.3°. Cross-sectional scanning transmission electron microscopy (STEM) samples were prepared using a focused ion beam (FIB, FEI Helios Nano 450F1) milling technique. The atomic and mesoscale structures of the cross-sectional HLO films were investigated by aberration-corrected STEM (GrandARM300CF, JEOL) operating at 300 kV with a probe-forming angle of ≈ 32 mrad. The high-angle annular dark field (HAADF) imaging mode with a detector inner angle of ≈ 68 mrad was used to obtain atomic structure images of the samples. To distinguish crystal structures, position-averaged convergent beam electron diffraction (PACBED)[19] and fast Fourier transform (FFT) analyses were subsequently conducted on the same regions observed by HAADF STEM.[21, 37] Further, the chemical compositions at various depths of

amorphous and crystalline HLO thin films were analyzed using depth profile X-ray photoelectron spectroscopy (XPS: ESCA 2000, MultiLab) with a monochromatic Al Kα X-ray source. The XPS spectra at different depths were recorded after etching with Ar for 300 s, 600 s, 900 s and 1200 s. The recorded spectra were calibrated using the C 1*s* signature response at 284.6 eV. The background type Shirley was used. For peak fit analysis, the Gaussian-Lorentzian product function (G/L: 30 %) was used, and the full-width at half-maximum (FWHM) of all synthetic peaks was constrained to be the same, fitted by the software CASAXPS 2.3.22PR1.0.

STEM combined with energy dispersive X-ray spectroscopy (EDX: JED-2300T, JEOL) was performed to analyze the elemental distribution in the samples at atomic resolution. The EDX instrument includes two Si-drift detectors with effective X-ray sensing areas of 100 mm^2 each, providing a large effective solid angle of ≈ 1.2 sr., which translates into an ≈ 10 % collection efficiency for the generated X-ray signals (4π sr.). Electron energy loss spectroscopy (EELS: Gatan GIF Quantum ER 965) spectrum imaging (SI) completed in HAADF STEM mode was used to perform energy loss near edge structure (ELNES) analysis of the O *K* edge for the cross-sectional HLO films. EELS SI datasets for the HLO samples were obtained under conditions of an accelerating voltage of 300 kV and an energy dispersion of 0.25 eV/ch for the energy loss ranges of 180–692 eV and 420–932 eV with a 5 mm entrance aperture. To obtain *A/B* ratio maps of the HLO films, a multiple linear / nonlinear least squares (M/NLLS) curve fitting approach[21, 37] was applied to the *A* and *B* peaks in the O *K* ELNES, which was implemented in the data processing software Gatan DigitalMicrograph®.

Polarization measurements: CSD-grown HLO thin films on Si (p++) substrates were further processed to fabricate Si/HLO/Mo capacitors. The top Mo (diameter: 100 μm) electrodes of the ferroelectric capacitors were deposited using room-temperature radio-frequency sputtering with a

dot pattern shadow mask. The electrical performance of the fabricated capacitors was characterized using a ferroelectric tester (Precision LC II, Radiant Technologies) under ambient conditions. Polarization vs. voltage (P vs. V) curves and ferroelectric currents were recorded with a frequency of 1 kHz by sweeping the input voltage of ± 25 V. Furthermore, the leakage and non-ferroelectric contributions were excluded using positive up negative down (PUND) measurements (detailed in supplementary information). An endurance test was performed using bipolar triangular pulses to extract P_r with PUND after cycling. In the retention test, after polling the HLO through triangular pulses with a width of 1 ms, the P_r from the polarization loop measured at 1 kHz was measured using PUND. The details of parameters used for PUND, endurance and retention tests are provided in the supplementary information.

Fabrication, characterization and simulation of NCFETs: ≈ 40 nm HLO [2-ME+Aq, 800 ^oC] thin films on silicon were further subjected to the deposition of dielectric Al_2O_3 layer (thickness: 10 nm) using ALD (Lucida D100, NCD Co., Ltd., Daejeon, Korea). This helps in stabilizing negative capacitance.[38] These HLO/Al_2O_3 film stacks were used in bottom gate top contact devices with ≈ 50 nm IGZO channel (dimensions: length/width: 10/15 µm/µm). All devices were characterized using I_D vs. V_{GS} at a constant drain-to-source bias (V_{DS}) of 1 V. The sweep rate of the V_{GS} ramp was ≈ 0.35 V/s with 50-mV step; forward and reverse voltage sweeps were performed to assess the I vs. V hysteresis. All curves were acquired using a semiconductor parameter analyzer (SCS-4200A, Keithley). For comparison, IGZO metal-oxide-semiconductor-field effect-transistors (MOSFETs) were fabricated with only the 10-nm Al_2O_3 layer in the gate stack. To gain more insights, numerical device simulations were carried out. The details of the simulation setup as well as the list of parameters are reported in the supplementary information (Table S23-S26). The same geometrical parameters of the actual device were employed in the simulated structure.

ASSOCIATED CONTENT

Supporting information

The Supporting Information is available free of charge at

Thermal analysis of HLO precursors; The variation of thickness of HLO on Si with RTA of 700 ^{o}C using 2-ME and 2-ME+Aq based precursors; Electron energy loss spectroscopy (EELS) analysis for ligand-induced impurity elements; Electron energy loss spectroscopy (EELS) analysis for ligand-induced impurity elements; Electron backscatter diffraction (EBSD) analysis for grain size measurement; Surface topography of HLO films; EDX elemental distribution mapping; Fast Fourier transform (FFT) pattern and position-averaged convergent beam electron diffraction (PACBED) pattern analyses; Chemical origin of oxygen vacancies in HLO films: x-ray photoelectron spectroscopic measurements; XPS peak fitting procedure and the tables containing peak position, FWHM and atomic fraction; XPS depth profiles of HLO thin films; Ferroelectric polarization measurements of Si/HLO/Mo; Effect of [2-ME+Aq] precursor aging on phase and ferroelectric behavior of HLO thin films; Description of positive up negative down (PUND) measurements; Description of endurance measurements; Stability of CSD-HLOs under electric field cycling

AUTHOR INFORMATION

Corresponding authors

Pavan Nukala − *Centre for Nano Science and Engineering, Indian Institute of Science, Bengaluru, 560012, India. Email: pnukala@iisc.ac.in*

Young-Min Kim − *Department of Energy Science, Sungkyunkwan University (SKKU), Suwon 16419, Republic of Korea. Email: youngmk@skku.edu*

Muhammad Ashraful Alam − *School of Electrical and Computer Engineering, Purdue University, West Lafayette, Indiana 47907, USA. Email: alam@purdue.edu*

Sunkook Kim − *Multifunctional Nano Bio Electronics Lab, School of Advanced Materials Science and Engineering, Sungkyunkwan University, Gyeonggi-do, Suwon 16419, Republic of Korea. Email: seonkuk@skku.edu*

Authors

Pavan Pujar − *Multifunctional Nano Bio Electronics Lab, School of Advanced Materials Science and Engineering, Sungkyunkwan University, Gyeonggi-do, Suwon 16419, Republic of Korea; Department of Ceramic Engineering, Indian Institute of Technology (IIT-BHU), Varanasi, Uttar Pradesh 221005, India; orcid.org/0000-0002-1012-7668*

Haewon Cho − *Multifunctional Nano Bio Electronics Lab, School of Advanced Materials Science and Engineering, Sungkyunkwan University, Gyeonggi-do, Suwon 16419, Republic of Korea; orcid.org/0009-0001-9925-7695*

Young-Hoon Kim − *Department of Energy Science, Sungkyunkwan University (SKKU), Suwon 16419, Republic of Korea.*

Nicolò Zagni − *Department of Engineering "Enzo Ferrari" (DIEF), University of Modena and Reggio Emilia, Modena 41125, Italy.*

Eunha Lee − *Analytical Engineering Group, Samsung Advanced Institute of Technology (SAIT), Samsung Electronics, Suwon, 16678 Republic of Korea.*

Srinivas Gandla − *Multifunctional Nano Bio Electronics Lab, School of Advanced Materials Science and Engineering, Sungkyunkwan University, Gyeonggi-do, Suwon 16419, Republic of Korea.*

Author Contributions

P.P., P.N., Y.-M.K., M.A.A., and S.K., conceived this work. P.P., H.C., and Y.-H.K. have performed the experiments. P.P., H.C., N.Z., and Y.-H.K. wrote the manuscript. P.P., H.C., Y.-H.K., N.Z., S.G., P.N., Y.-M.K., M.A.A., and S.K. conducted investigations. P.P. and H.C. prepared HLO samples for TEM analyses. Y.-H.K., and E.L. performed TEM analyses. P.P., and H.C., fabricated NCFETs and characterized them. N.Z. conducted simulation of NCFETs. All authors contributed to the discussion and analysis of the results.

Notes

The authors declare that they have no known competing financial interests.

ACKNOWLEDGEMENTS

This research was supported by the National Research Foundation of Korea (NRF-2021R1I1A1A01060065, NRF-2020R1A2C1006207). This study was also supported by the SKKU Research Fellowship Program of Sungkyunkwan University and the National Research Foundation of Korea (2021R1I1A1A01060078). The authors acknowledge Brain Korea for providing postdoctoral fellowship to PP The use of TEM instrument was supported by Advanced Facility Center for Quantum Technology in SKKU. PN would like to acknowledge the institute of eminence start up grant from Indian Institute of Science (IISc) Bangalore, and SERB-SRG/2021/00285/ES.

REFERENCES

1. Cheema SS, Kwon D, Shanker N, Dos Reis R, Hsu S-L, Xiao J*, et al.* Enhanced ferroelectricity in ultrathin films grown directly on silicon. *Nature* **580**, 478-482 (2020).

2. Lee H-J, Lee M, Lee K, Jo J, Yang H, Kim Y*, et al.* Scale-free ferroelectricity induced by flat phonon bands in HfO_2. *Science* **369**, 1343-1347 (2020).

3. Wei Y, Nukala P, Salverda M, Matzen S, Zhao HJ, Momand J*, et al.* A rhombohedral ferroelectric phase in epitaxially strained $Hf_{0.5}Zr_{0.5}O_2$ thin films. *Nature materials* **17**, 1095-1100 (2018).

4. Chen H, Zhou X, Tang L, Chen Y, Luo H, Yuan X*, et al.* HfO_2-based ferroelectrics: From enhancing performance, material design, to applications. *Applied Physics Reviews* **9**, 011307 (2022).

5. Hsain HA, Lee Y, Materano M, Mittmann T, Payne A, Mikolajick T*, et al.* Many routes to ferroelectric HfO_2: A review of current deposition methods. *Journal of Vacuum Science & Technology A: Vacuum, Surfaces, and Films* **40**, 010803 (2022).

6. Schenk T, Godard N, Mahjoub A, Girod S, Matavz A, Bobnar V*, et al.* Toward thick piezoelectric HfO_2-based films. *physica status solidi (RRL)–Rapid Research Letters* **14**,1900626 (2020).

7. Starschich S, Griesche D, Schneller T, Waser R, Böttger U. Chemical solution deposition of ferroelectric yttrium-doped hafnium oxide films on platinum electrodes. *Applied physics letters* **104**, 202903 (2014).

8. Riedel S, Polakowski P, Müller J. A thermally robust and thickness independent ferroelectric phase in laminated hafnium zirconium oxide. *Aip Advances* **6**, 095123 (2016).

9. Yun Y, Buragohain P, Li M, Ahmadi Z, Zhang Y, Li X*, et al.* Intrinsic ferroelectricity in Y-doped HfO_2 thin films. *Nature Materials* **21**, 903-909 (2022).

10. Cho D-Y, Jung HS, Yu I-H, Yoon JH, Kim HK, Lee SY*, et al.* Stabilization of tetragonal HfO_2 under low active oxygen source environment in atomic layer deposition. *Chemistry of Materials* **24**, 3534-3543 (2012).

11. Pujar P, Cho H, Gandla S, Naqi M, Hong S, Kim S. Sub-thermionic negative capacitance field effect transistors with solution combustion-derived $Hf_{0.5}Zr_{0.5}O_2$. *Advanced Functional Materials* **31**, 2103748 (2021).

12. Masuduzzaman M, Xie S, Chung J, Varghese D, Rodriguez J, Krishnan S*, et al.* The origin of broad distribution of breakdown times in polycrystalline thin film dielectrics. *Applied Physics Letters* **101**, 153511 (2012).

13. Böttger U, Starschich S, Griesche D, Schneller T. Dopants in chemical solution-deposited HfO_2 films. *Ferroelectricity in Doped Hafnium Oxide: Materials, Properties and Devices*. Elsevier 127-143 (2019).

14. Starschich S, Boettger U. An extensive study of the influence of dopants on the ferroelectric properties of HfO 2. *Journal of Materials Chemistry C* **5**, 333-338 (2017).

15. Li P, Chen IW, Penner-Hahn JE. Effect of dopants on zirconia stabilization—an X-ray absorption study: I, trivalent dopants. *Journal of the American Ceramic Society* **77**, 118-128 (1994).

16. Kao M-Y, Sachid AB, Lin Y-K, Liao Y-H, Agarwal H, Kushwaha P*, et al.* Variation caused by spatial distribution of dielectric and ferroelectric grains in a negative capacitance field-effect transistor. *IEEE Transactions on Electron Devices* **65**, 4652-4658 (2018).

17. Park JW, Kang BH, Kim HJ. A review of low-temperature solution-processed metal oxide thin-film transistors for flexible electronics. *Advanced Functional Materials* **30**, 1904632 (2020).

18. Pasquarelli RM, Ginley DS, O'Hayre R. Solution processing of transparent conductors: from flask to film. *Chemical Society Reviews* **40**, 5406-5441 (2011).

19. Kim YH, Yang SH, Jeong M, Jung MH, Yang D, Lee H*, et al.* Hybrid deep learning crystallographic mapping of polymorphic phases in polycrystalline $Hf_{0.5}Zr_{0.5}O_2$ thin films. *Small* **18**, 2107620 (2022).

20. Park MH, Schenk T, Fancher CM, Grimley ED, Zhou C, Richter C*, et al.* A comprehensive study on the structural evolution of HfO_2 thin films doped with various dopants. *Journal of Materials Chemistry C* **5**, 4677-4690 (2017).

21. Kang S, Jang W-S, Morozovska AN, Kwon O, Jin Y, Kim Y-H*, et al.* Highly enhanced ferroelectricity in HfO_2-based ferroelectric thin film by light ion bombardment. *Science* **376**, 731-738 (2022).

22. Lee J, Song MS, Jang WS, Byun J, Lee H, Park MH*, et al.* Modulating the ferroelectricity of hafnium zirconium oxide ultrathin films via interface engineering to control the oxygen vacancy Distribution. *Advanced Materials Interfaces* **9**, 2101647 (2022).

23. Shim J-H, Kang H, Lee S, Kim Y-M. Utilization of electron-beam irradiation under atomic-scale chemical mapping for evaluating the cycling performance of lithium transition metal oxide cathodes. *Journal of Materials Chemistry A* **9**, 2429-2437 (2021).

24. Kim Y, Jeong M, Byun J, Yang S-H, Choi W, Jang W-S*, et al.* Atomic-scale identification of invisible cation vacancies at an oxide homointerface. *Materials Today Physics* **16**, 100302 (2021).

25. Stemmer S, Chen Z, Zhu W, Ma T. Electron energy-loss spectroscopy study of thin film hafnium aluminates for novel gate dielectrics. *Journal of microscopy* **210**, 74-79 (2003).

26. Mizoguchi T, Saitoh M, Ikuhara Y. First-principles calculation of oxygen K-electron energy loss near edge structure of HfO_2. *Journal of Physics: Condensed Matter* **21**, 104212 (2009).

27. Wilk G, Muller D. Correlation of annealing effects on local electronic structure and macroscopic electrical properties for HfO_2 deposited by atomic layer deposition. *Applied physics letters* **83**, 3984-3986 (2003).

28. Blanco-Portals J, Torruella P, Baiutti F, Anelli S, Torrell M, Tarancón A*, et al.* WhatEELS. A python-based interactive software solution for ELNES analysis combining clustering and NLLS. *Ultramicroscopy* **232**, 113403 (2022).

29. Schenk T, Bencan A, Drazic G, Condurache O, Valle N, Adib BE*, et al.* Enhancement of ferroelectricity and orientation in solution-derived hafnia thin films through heterogeneous grain nucleation. *Applied Physics Letters* **118**, 162902 (2021).

30. Nukala P, Antoja-Lleonart J, Wei Y, Yedra L, Dkhil B, Noheda B. Direct epitaxial growth of polar $(1–x)HfO_2–(x)ZrO_2$ ultrathin films on silicon. *ACS applied electronic materials* **1**, 2585-2593 (2019).

31. Su KB, Dam HS, Taehwan M, Lee YH, Park HW, Lee YB*, et al.* A Comparative study on the ferroelectric performances in atomic layer deposited $Hf_{0.5}Zr_{0.5}O_2$ thin films using tetrakis (ethylmethylamino) and tetrakis (dimethylamino) precursors. *Nanoscale Research Letters* **15**, (2020).

32. Huang K-W, Yi S-H, Jiang Y-S, Kao W-C, Yin Y-T, Beck D*, et al.* Sub-7-nm textured ZrO_2 with giant ferroelectricity. *Acta Materialia* **205**, 116536 (2021).

33. Scott JF, Araujo C, Meadows HB, McMillan L, Shawabkeh A. Radiation effects on ferroelectric thin-film memories: Retention failure mechanisms. *Journal of applied physics* **66**, 1444-1453 (1989).

34. Cao W, Banerjee K. Is negative capacitance FET a steep-slope logic switch? *Nature communications* **11**, 1-8 (2020).

35. Deng S, Liu Z, Li X, Ma T, Ni K. Guidelines for ferroelectric FET reliability optimization: Charge matching. *IEEE Electron Device Letters* **41**, 1348-1351 (2020).

36. Nukala P, Ahmadi M, Wei Y, De Graaf S, Stylianidis E, Chakrabortty T*, et al.* Reversible oxygen migration and phase transitions in hafnia-based ferroelectric devices. *Science* **372**, 630-635 (2021).

37. Jang W-S, Jin Y, Kim Y-H, Yang S-H, Kim SJ, Hong JA*, et al.* Site-selective doping mechanisms for the enhanced photocatalytic activity of tin oxide nanoparticles. *Applied Catalysis B: Environmental* **305**, 121083 (2022).

38. Zagni N, Alam MA. Reliability physics of ferroelectric/negative capacitance transistors for memory/logic applications: An integrative perspective. *Journal of Materials Research* **36**, 4908-4918 (2021).